Flow Measurement and Instrumentation 78 (2021) 101876

Contents lists available at ScienceDirect

Flow Measurement and Instrumentation

journal homepage: http://www.elsevier.com/locate/flowmeasinst

Numerical modeling and experimental verification of a low fluid flow inductive flowmeter

P. Drexler [a,1], P. Fiala [b,2,*], R. Kadlec [a,3], P. Londak [a,4], T. Madrova [a,5], M. Klima [a,6], J. Zukal [a,7]

[a] Dept. of Theoretical and Experimental Electrical Engineering, Brno University of Technology, Technická 12, 616 00, Brno, Czech Republic
[b] SIX Research Center, Brno University of Technology, Technická 12, 616 00, Brno, Czech Republic

ARTICLE INFO

Keywords:
Magnetohydrodynamics
Fluid flow measurement
Finite element methods
Turbulent media
Coupled modeling
Plasma

ABSTRACT

The article discusses modeling procedures to capture the physical and chemical processes present in operational measurement with a high-precision inductive flowmeter. In this context, a theoretical model and a numerical solution are proposed. Exploiting the combined finite element method (FEM) and the finite volume method (FVM), we prepared numerical models of multiple variants of the flowmeter and computed the output voltage on the device's electrodes. The model joins together the magnetic, electric, and current fields; a flow field; and a physical-chemical nonlinear ion model. The results were obtained by means of the FEM/FVM in ANSYS software and verified via experimental testing.

1. Introduction

The current trend of implementing various precise industrial measurement techniques [1–3] involves multiple activities, such as performing parametric measurement or special monitoring of liquid, semi-liquid, and solid commodities before transportation, and designing methods or systems to facilitate flow velocity measurement [4–6]. This group of substances comprises, for example, organic and inorganic liquids characterized by different degrees of corrosivity [7], low temperature fluids (−180 °C to - 196 °C), and fluid gases (including, for instance, argon and nitrogen). The actual liquid flow can be advantageously measured with inductive flowmeters [8], whose design and parametric description embody relatively complex tasks in terms of the analysis of the modeling results and its accuracy. The equivalent models are both lumped parameter ones [11] and those based on solving partial differential equations [9,10]. We designed and verified an applicable model, utilizing precise flow evaluation at a mean speed of v = 0.1–10 m/s.

The full electro-magneto-hydro-dynamical (EMHD) model of an inductive flowmeter is a coupled problem, comprising coupled electric, magnetic, and fluid flow fields together with electric circuit and physical-chemical (ion) models; the relevant geometrical structure is demonstrated in Fig. 1. The designed physical and mathematical models are solvable from different perspectives.

Several methods for measuring the flow rate of small amounts or low velocities of liquids are presently being developed and characterized. An interesting approach was proposed by Prasan [12], who measured fluid flow by compensating the pressure drop across the ends of the measuring unit using a compensation pump. The flow-induced pressure drop is balanced by a feedback control loop. This is the type of measurement being balanced to zero deviation. In small flow measurements, for example, Chen et al. [13] outlined an application for space research; in this context, it is important to stress the necessity of managing the measurement of fuel flow in microgravity conditions. Ultrasonic measurements offer the advantages of non-invasive and immobile component structures as well as fast responses to the detection of bidirectional flow, whose applications in space exploration have already been described. To avoid the drawbacks of pulsed ultrasonic measuring

* Corresponding author. Tel.: +420541146276.
E-mail address: fialap@feec.vutbr.cz (P. Fiala).
[1] drexler@feec.vutbr.cz, www.utee.feec.vutbr.cz.
[2] fialap@feec.vutbr.cz, www.utee.feec.vutbr.cz.
[3] kadlec@feec.vutbr.cz, www.utee.feec.vutbr.cz.
[4] xlonda00@stud.feec.vutbr.cz, www.utee.feec.vutbr.cz.
[5] xmadro05@stud.feec.vutbr.cz, www.utee.feec.vutbr.cz.
[6] klimam@feec.vutbr.cz, www.utee.feec.vutbr.cz.
[7] xzukal03@stud.feec.vutbr.cz, www.utee.feec.vutbr.cz.

https://doi.org/10.1016/j.flowmeasinst.2020.101876
Received 30 April 2020; Received in revised form 20 November 2020; Accepted 12 December 2020
Available online 6 January 2021

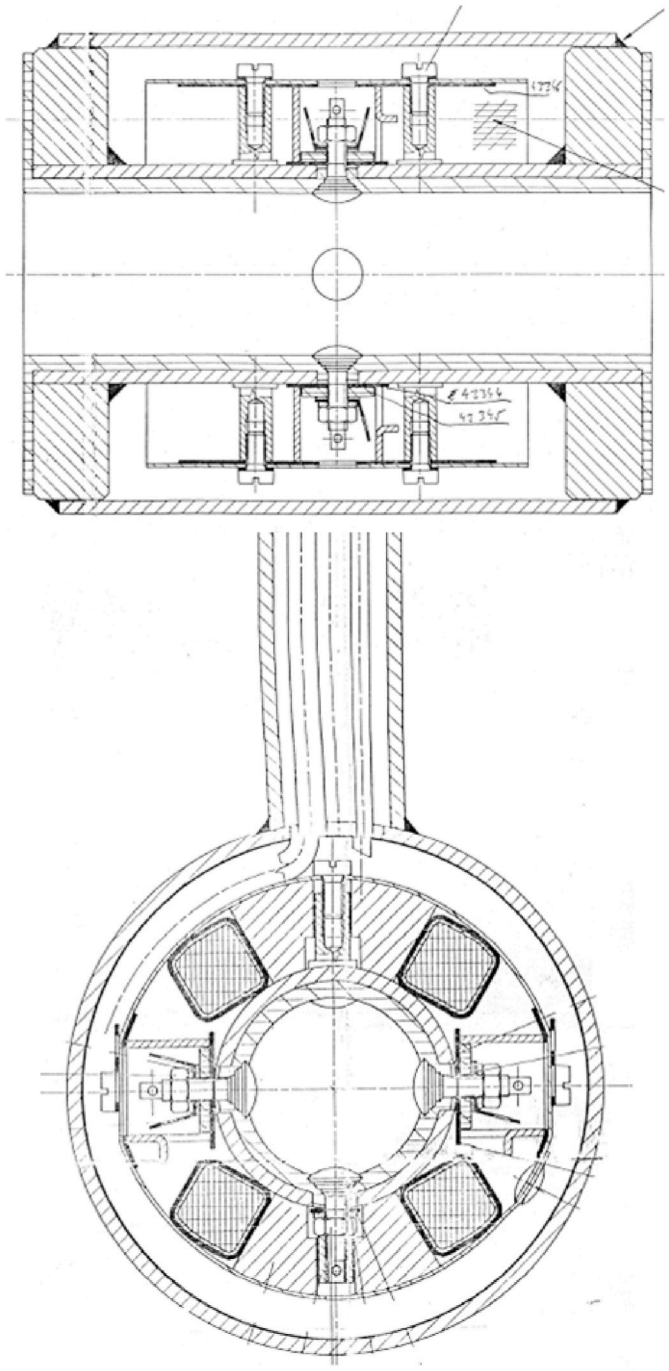

Fig. 1. The structure of an inductive flowmeter.

configurations, the study presents flow measurement via continuous propagation of ultrasonic waves to meet the requirements of a large measurement range and high accuracy. Article [14] then compares two methods for runoff measurement in chimneys to determine the errors exhibited by the techniques in the presence of cyclone flow (a turbulent environment). One of these procedures, based on speed measurements with a Pitot tube in a grid of points, is the standard reference method according to EN ISO 16911–1. The other approach, ultrasonic measurement, is often employed as an automated measuring system pursuant to EN ISO 16911–2. The methods involve the analysis of several typical reservoir configurations, and the flow field in the reservoirs is obtained by using validated computational fluid dynamics (CFD) modeling exploiting OpenFoam software. The researchers emphasize that possible errors in the standard reference method occurring in the presence of a cyclonic flow are significant compared to the requirements of the EU ETS. Thus, procedures associated with numerical modeling are shown as indispensable in solving non-trivial problems.

Magneto-inductive flowmeters play an important role in the measurement of conductive, partially conductive, and dielectric liquids [15]. Approximately 30–40% of all applications require flow sensors that utilize alternating EMG field, due to the physical properties of the material being monitored or the hydraulic effects. This aspect affects the measurement of the flow rate of a liquid with a high solid content or a very low conductivity. Magnetic inductive flow sensors have proved reliable in most sectors on a long-term basis; in the given segment, however, magnetic inductive flow sensors without alternating EMG fields often reach their very limits, which leads to uneven or noisy initial signals and inaccurate and/or inadequately reproducible processing of the measurement evaluation data in the ongoing process.

An inductive flow sensor has certain drawbacks, including that the application of point electrodes (IFS-SE) is sensitive to the shape of the flow profile and that the device's usability remains limited to measuring the axially symmetric single-phase flows in a circular tube. The sensor therefore must align with not fully developed flow profiles. To improve the accuracy, the authors of paper [16] designed an inductive flow sensor with a pair of arcuate electrodes embedded in the inner surface of the insulating part of the pipe.

In [17], an electric charge induced on a ring sensor with different geometric sizes from a single particle having a single charge was described and mathematically modeled. The spatial sensitivity of the sensor was then derived from a numerical solution obtained via ANSYS finite element analysis software. The influence of the geometric size of the sensor on the spatial sensitivity was also investigated, and the relevant basic theory and effect of spatial filtering were quantitatively analyzed. The time-frequency response characteristics were obtained and derived. In the discussed context, a suitable mathematical model and its detailed analysis have proved necessary to achieve extreme flowmeter requirements.

Selecting and using an optimum non-destructive flow measurement method (range of measured mean velocity $v = 0.01–1.0$ mm/s) within dendrology and identifying the issues to be resolved in connection with such activities are the central problems characterized in a dedicated article by Čermák [18]. The paper describes methods for measuring several variables, including sap flow rates, which are commonly utilized to investigate transpiration.

The research in this subdomain of flow measurement has expanded further also through the advanced procedure outlined in Ref. [19], namely, the "Linear Heat Balance (LHB) method"; the approach exploits an exact (physically correct) equation analytically derived from the basic convection heat transfer equation. More concretely, the paper defines a semi-destructive method for measuring the flow rate of liquids in a tree xylem by using heat balance and the measured temperature differences around a continuously heated point source of a heat-needle. The novel formula is analyzed and verified via numerical simulation (the finite element method), and the LHB method is demonstrated on experimentally measured data.

The procedure described below brings a significant shift in the accuracy of the non-destructive measurement of the flow rate in the range of $v = 0.01–1$ mm/s. The research presented above indicates the need to characterize in detail the electrodynamics of the fluid flow, including the chemical composition and effects on the measured quantity. This problem is further discussed in relation to the physical-mathematical model formulated and tested for use with the finite element method (FEM).

A viable approach to modeling the physical properties rests in the analytical solution of the flowmeter model, exploiting formulation via concentrated parameters [11,20] and containing the necessary electronics [20]. An alternative analysis then relies on detailed formulation and assembly variants of the numerical bound model [21]. Furthermore,

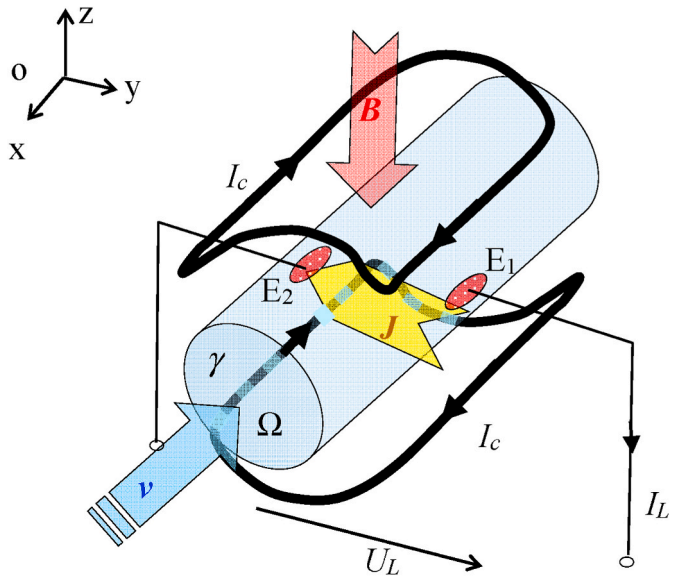

Fig. 2. The principal configuration of an inductive flowmeter.

the path following the finite element plus finite volume methods to formulate, describe, and solve the inductive flowmeter model with distributed parameters is selected.

2. Mathematical-physical model

The electromagnetic part of the flowmeter is derived from the reduced Maxwell equations

$$curl\ \ \mathbf{H}=0, \tag{1}$$

$$div\ \ \mathbf{B}=0, \tag{2}$$

where $\boldsymbol{H}$ is the magnetic field intensity vector and $\boldsymbol{B}$ denotes the magnetic flux density vector

$$\mathbf{B}=\mu_0\mathbf{H}, \tag{3}$$

$$\mathbf{J}=\gamma\mathbf{E}, \tag{4}$$

$$curl\ E=0, \tag{5}$$

$$divJ=0, \tag{6}$$

where $\boldsymbol{E}$ is the electric field intensity vector, $\boldsymbol{J}$ denotes the current density vector, μ_0 stands for the permeability of vacuum, and γ represents the specific conductance of the measured liquid.

The vector functions of the electric and the magnetic fields are expressed by means of the scalar electric φ_e and magnetic φ_m potentials

$$E=-\text{grad}\ \ \varphi_e, \tag{7}$$

$$H=-\text{grad}\ \ \varphi_m. \tag{8}$$

The final current density $\boldsymbol{J}$ from (4) is influenced by the velocity $\boldsymbol{v}$ of the flowing ion solution and the outer magnetic field

$$J=\gamma(E+v\times B). \tag{9}$$

If the electrodes E_1 and E_2 exhibit different electric potentials (Fig. 2), the current density $\boldsymbol{J}$ is formed in the Ω area, according to (9), and the current I_L flows in the ion solution, as follows:

$$I_L=\iint_{S_e}\mathbf{J}\cdot d\mathbf{S},$$

$$I_L=\iint_{S_e}\gamma(\mathbf{E}+v\times\mathbf{B})\cdot d\mathbf{S}, \tag{10}$$

where S_e is the oriented area of the electrodes E_1 and E_2 into the space Ω. Equation (10) comprises the electric field intensity $\boldsymbol{E}$ for the ion solution

$$|\mathbf{E}|<<|\mathbf{v}\times\mathbf{B}|; \tag{11}$$

we therefore disregard the influence of the electric field intensity. The specific force f affecting the moving charge q is

$$f=\mathbf{J}\times\mathbf{B}, \tag{12}$$

and the force in the whole area Ω is

$$F=\iiint_{\Omega}J\times B\ \ dV. \tag{13}$$

The voltage between the flowmeter electrodes E_1, E_2 is obtained from

$$U_L=\int_{E_1}^{E_2}\mathbf{E}\cdot d\ell, \tag{14}$$

where the electric field intensity $\boldsymbol{E}$ is derived out of the force $\boldsymbol{F}$, which affects a charge q; the voltage then equals

$$U_L=\int_{E_1}^{E_2}\frac{F}{q}\cdot d\ell. \tag{15}$$

If a charge is substituted for the equation of the steady state current I_L, we have

$$U_L=\int_{E_1}^{E_2}\frac{\iiint_{\Omega}J(v)\times B\ \ dV}{I_L\ \ \Delta\ell}\cdot(v_{io}+v)\cdot d\ell, \tag{16}$$

where $\Delta\ell$ is the length element in the direction between the electrodes E_1 and E_2; and v_{io} denotes the ion velocity in the lengthwise direction between E_1 and E_2. The current density $\boldsymbol{J}(v)$ depends on the immediate ion velocity between E_1 and E_2. After reduction, the voltage on the flowmeter electrodes equals

$$U_L=\iiint_{\Omega}\left(\frac{J(v)}{I_L}\times B\right)\cdot(v_{io}+v)\ \ dV \tag{17}$$

The fluid flow velocity distribution model is derived for an incompressible fluid as

$$divv=0; \tag{18}$$

with a stable flow, we have

$$div\rho v=0 \tag{19}$$

from the law of conservation of energy, where ρ is the specific density. We assume the turbulent flow

$$curl\ \ \nu=2\omega, \tag{20}$$

where ω denotes the angular velocity of fluid. By utilizing Stokes' theorem and the Helmholtz theorem for the moving particles to obtain the continuity equation, we can formulate from the balance of forces the Navier-Stokes equation for the fluid element,

$$\frac{\partial v}{\partial t}+v\cdot gradv=A-\frac{1}{\rho}grad\ p+\upsilon\cdot\Delta v, \tag{21}$$

where $\boldsymbol{A}$ is the external acceleration, $\boldsymbol{\nu}$ the kinematic viscosity, and p the pressure. In formula (21), we can substitute the pressure losses

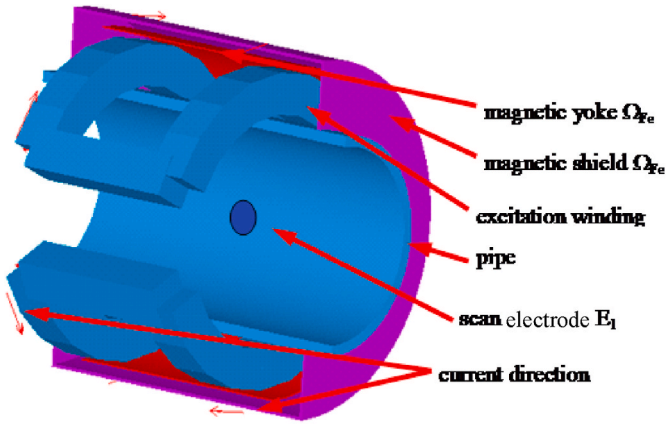

Fig. 3. A geometric model of the flowmeter body.

$$\begin{aligned} grad\ p = &-\left(K_x\ \rho\ v_x|v| + \frac{f_r}{D_h}\rho\ v_x|v| + C_x\mu_p v_x\right)u_x \\ &-\left(K_y\ \rho\ v_y|v| + \frac{f_r}{D_h}\rho\ v_y|v| + C_y\mu_p v_y\right)u_y, \\ &-\left(K_z\ \rho\ v_z|v| + \frac{f_r}{D_h}\rho\ v_z|v| + C_z\mu_p v_z\right)u_z \end{aligned} \tag{22}$$

where K denotes the suppressed pressure losses, f_r the resistance coefficient, D_h the hydraulic diameter, C the air permeability of the system, μ_p the dynamic viscosity, and $\boldsymbol{u}$ the unit vector of the Cartesian coordinate system. The resistance coefficient is obtained from the Boussinesq theorem [22–28] as

$$f_r = a\mathrm{R_e}^{-b} \tag{23}$$

where a, b are the coefficients from Ref. [20]. The magnetic field, expressed in (17) by the flux density $\boldsymbol{B}$, is gained from the Biot-Savart law via the differential scalar magnetic potential (DSP),

$$T = \frac{1}{4\pi}\int_{\Omega}\frac{J_c \times R}{|R|^3}\ dV \tag{24}$$

where $\boldsymbol{R}$ is the positional vector between the point where we seek the magnetic field intensity $\boldsymbol{T}$ and the point where the magnetic field source is I_c (Fig. 2), characterized by the current density $\boldsymbol{J}_c$. The magnetic field intensity $\boldsymbol{H}$ in the area Ω can be expressed as

$$H = T - grad\ \varphi_m, \tag{25}$$

where $\boldsymbol{T}$ is the above (estimated) magnetic field intensity. The boundary conditions are

$$n \cdot \mu_0\mu_r\ (T - grad\varphi_m) = 0,\ \text{on the boundary}\ \Gamma_{\mathrm{Fe}-0}, \tag{26}$$

where $\boldsymbol{n}$ is the normal vector and $\Gamma_{\mathrm{Fe}\text{-}0}$ denotes the interface between the areas Ω_{Fe} and Ω in Fig. 3. The continuity of the tangential components of the magnetic field intensity on the interface between the area and a ferromagnetic material is

$$n \times\ (T - grad\varphi_m) = 0,\ \text{on the boundary}\ \Gamma_{\mathrm{Fe}-0}. \tag{27}$$

With the help of formulas (1), (2), and (5), we yield

$$div\ \ \mu_0\mu_r T - div\ \ \mu_0\mu_r \mathrm{grad}\varphi_{\mathrm{m}} = 0 \tag{28}$$

Equation (28) is discretized by means of an approximation of the scalar magnetic potential

$$\varphi_m = \sum_{k=1}^{N_\varphi}\phi_{mk}W_k(x,y,z),\ \forall(x,y,z) \subset \Omega, \tag{29}$$

where ϕ_m is the nodal value of the scalar magnetic potential and W_k denotes the base function. We obtain the semidiscrete solution via approximating (29) within formula (28) and through the use of the Galerkin method:

$$\sum_{j=1}^{N_\varphi} -\int_{\Omega}\mu\ t_j \cdot gradW_i + \mu\ grad\ \phi_{mj} \cdot gradW_i\ \ d\Omega = 0 \quad ,\ \ i = 1,..,N_\phi \tag{30}$$

where t_j represents the nodal value of the known magnetic field intensity in the mesh. It is possible to write the above equation (30) briefly as

$$-\left[k_{Tij}\right] + \left[k_{ij}\right]\{\phi\} = 0 \qquad i,j = 1,..,N_\phi \tag{31}$$

The coefficients for (31) are expressed as

$$k_{Tij}^{em} = -\int_{\Omega^e}\mu^e\ t_j \cdot gradW_i d\Omega \quad i,j = 1,..,N_e, \tag{32}$$

$$k_{ij}^{em} = -\int_{\Omega^e}\mu^e\ grad\ \phi_j \cdot gradW_i\ \ d\Omega \tag{33}$$

where μ^e is the material permeability of a selected element and N_e denotes the number of mesh elements. The equation system changes into the formula

$$-\left[k_{Tij}^{em}\right] + \left[k_{ij}^{em}\right]\{\phi\} = 0 \quad e = 1,..,N_e; \tag{34}$$

this system can then be solved (34) by utilizing standard algorithms.

The solution exploiting the DSP comprises two processes: First, we express the distribution of the magnetic field intensity T from the current sources according to (24), with respect to the boundary conditions (26) and (27) in the area Ω_{Fe}. Second, based on the previous step, we solve the distribution of the magnetic intensity H according to (25). Assuming that the cross-section of the wire S of the exciting coil's winding is constant, we can write for the current density in the coil winding

$$J = \frac{I}{S}\ n, \tag{35}$$

where $\boldsymbol{n}$ is the normal component related to the cross-section of a wire having the area S. The model of the electric or current field is formulated from equations (3), (4), (6) and (7):

$$\gamma\ div\ \ grad\varphi_{\mathrm{e}} = 0. \tag{36}$$

The boundary conditions are

$$n \cdot \gamma\ (grad\varphi_e) = 0, \text{at}\ \Gamma_{\mathrm{E}-\mathrm{k}}, \tag{37}$$

where $\boldsymbol{n}$ is the normal vector of the surface of an electrode E, and $\Gamma_{\mathrm{E}\text{-}\mathrm{k}}$ denotes the interface between the fluid and an electrode E. The continuity of the tangential components of the electric field intensity on the interface is

$$n \times\ (grad\varphi_e) = 0 \text{ at } \Gamma_{\mathrm{E}-\mathrm{k}}. \tag{38}$$

The scalar electric potential can be approximated similarly to the procedure in formula (29); by exploiting (29), (36), and the Galerkin method, we then obtain the semidiscrete solution

$$\sum_{j=1}^{N_\varphi} -\int_{\Omega}\gamma\ grad\ \phi_{ej} \cdot gradW_i\ \ d\Omega = 0 \quad ,\ \ i = 1,..,N_\phi \tag{39}$$

where ϕ_{ej} is the nodal value of the scalar electric potential in a mesh. equation (39) can be written with the help of

$$\left[k'_{ij}\right]\{\phi\} = 0 \qquad i,j = 1,..,N_\phi. \tag{40}$$

The coefficients for (40) are

$$k_{ij}^{Je} = -\int_{\Omega^e} \gamma^e \; grad\, \phi_{ej} \cdot grad W_i \; d\Omega \tag{41}$$

where γ^e is the specific conductivity of fluid in the static state of the selected element. The equation system changes into

$$\left[k_{ij}^{Je}\right]\{\phi\} = 0 \quad e = 1, .., N_e \tag{42}$$

where N_e is the number of mesh elements. The model of the velocity field is formulated from the steady-state stability condition, expressed as

$$\int_{\Omega} f d\Omega + \int t d\Gamma = 0 \tag{43}$$

where $\boldsymbol{f}$ denotes the specific forces in the area Ω, and $\boldsymbol{t}$ represents the pressures, tensions, and shear stresses on the interface of the area Γ. By utilizing transformation into local coordinates, we obtain the differential form for the static equilibrium,

$$f + div^2\, T_v = 0, \tag{44}$$

where div^2 stands for the tensor quantity operator *div*, and $\boldsymbol{T_v}$ denotes the internal tension tensor

$${}^2T_v = \begin{bmatrix} X_x & X_y & X_z \\ Y_x & Y_y & Y_z \\ Z_x & Z_y & Z_z \end{bmatrix} \tag{45}$$

where *X*, *Y*, *Z* are the stress components acting on the elements of the area Ω. A form of the specific force from (18)-(21) can be added to the static equilibrium condition; this form is obtained via the external acceleration $\boldsymbol{A}$, via the pressure losses and shear stresses τ. We have

$$\rho\left(\frac{\partial v}{\partial t} + v \cdot gradv\right) - \rho A - \sum_{\ell=1}^{N_s} F_\ell + div^2\, T_v = 0 \tag{46}$$

where F_ℓ are the discrete forces. The model covering the forces, viscosity, and pressure losses is expressed as

$$\rho\left(\frac{\partial v}{\partial t} + v \cdot gradv\right) - \rho A - \sum_{\ell=1}^{N_s} F_\ell + grad\, p - v \cdot \Delta v = 0 \tag{47}$$

Equation (21) can be discretized through an approximation of the velocity *v* and acceleration *a*:

$$v = \sum_{k=1}^{N_\varphi} \boldsymbol{\nu}_{vk} W_k(x,y,z), \;\; \forall (x,y,z) \subset \Omega, \;\; \forall (x,y,z) \subset \Omega,$$

$$a = \sum_{k=1}^{N_\varphi} \boldsymbol{\alpha}_{vk} W_k(x,y,z), \;\; \forall (x,y,z) \subset \Omega, \tag{48}$$

where v_v, a_v are the immediate node values, *W* denotes the base function, and N_φ represents the number of mesh nodes. By approximating (47) and utilizing the Galerkin principle from (48), we obtain the semi-discrete solution

$$\begin{aligned} &\int_\Omega W_j \left[\rho\left(\sum_{i=1}^{N_v} W_i \frac{\partial v_{vi}}{\partial t} + \sum_{i=1}^{N_v} W_i v_{vi} \cdot gradv_{vi}\right) + \sum_{i=1}^{N_v} W_i grad\, p_i \right. \\ &\left. -\rho \sum_{i=1}^{N_v} W_i A_{vi} - \sum_{i=1}^{N_v} W_i \sum_{\ell=1}^{N_s} F_{\ell i}\right] d\Omega \quad - \int_\Omega W_j \left[\sum_{i=1}^{N_v} W_i divv \cdot gradv_{vi}\right] d\Omega \\ &- \int_\Gamma W_j \left[\sum_{i=1}^{N_v} W_i X_i\right] d\Gamma = 0 \quad j = 1, .., N_v, \end{aligned} \tag{49}$$

where *X* denotes the known conditions on the interface of the area. We substitute the pressure losses in (49) for the function (22), yielding the flowing medium model

$$\begin{aligned} &\rho \int_\Omega W_j W_i d\Omega \frac{dv_{vi}}{dt} + \rho \int_\Omega W_j v_{vi} \cdot \left(\frac{dW_i}{dx} u_x + \frac{dW_i}{dy} u_y + \frac{dW_i}{dz} u_z\right) d\Omega\, v_{vi} \\ &+ \int_\Omega W_j \cdot \left(\frac{dW_i}{dx} u_x + \frac{dW_i}{dy} u_y + \frac{dW_i}{dz} u_z\right) d\Omega\, p_i \\ &-\rho \int_\Omega W_j d\Omega\, A_i - \int_\Omega W_j d\Omega\, F_{\ell i} \\ &- \int_\Omega \left(\frac{dW_j}{dx} + \frac{dW_j}{dy} + \frac{dW_j}{dz}\right) v_i \cdot \left(\frac{dW_i}{dx} u_x + \frac{dW_i}{dy} u_y + \frac{dW_i}{dz} u_z\right)_i d\Omega\, v_{vi}. \\ &- \int_\Gamma W_j d\Gamma\, X_i = 0 \quad i,j = 1, .., N_v \end{aligned} \tag{50}$$

The boundary conditions are

$$n \cdot (v) = 0 \text{ at } \Gamma_{vr1}, \tag{51}$$

where $\boldsymbol{n}$ is the normal vector to the direction of the fluid flow, and $\Gamma_{vr1} \subset \Gamma_{vr}$ denotes the interface between the fluid and the solid parts of the flowmeter. We have

$$n \cdot (p) = 0 \text{ on the boundary } \Gamma_{vr}, \tag{52}$$

where $\Gamma_{vr2} \subset \Gamma_{vr}$ is the interface between the liquid and the solid parts of the flowmeter. The system of equation (50) can now be written as

$$\begin{aligned} &\left[C_{ij}^f\right]\left\{\frac{dv_{vi}}{dt}\right\} + \left[K_{ij}^{sx} - K_{ij}^{Fx}\right]\{v_{vi}\} + \left[K_{ij}^{cx}\right] p_i = \left[K_{ij}^{gx}\right]\{A_i\} + \left[F_{ij}^{bx}\right]\{F_{\ell i}\} \\ &+ \left[F_{ij}^{sx}\right]\{X_i\}\; i,j = 1, .., N_v \end{aligned} \tag{53}$$

The matrices C_{ij}^f, K_{ij}^{sx}, K_{ij}^{Fx}, K_{ij}^{cx}, K_{ij}^{gx}, F_{ij}^{bx}, K_{ij}^{Fx}, F_{ij}^{sx} relate to the coefficients of the system of equation (49); we can rewrite the form for an element of mesh into

$$\begin{aligned} &\left[C_e^f\right]\left\{\frac{dv_{vi}}{dt}\right\} + \left[K_e^{sx} - K_e^{Fx}\right]\{v_{vi}\} + \left[K_e^{cx}\right] p_i = \left[K_e^{gx}\right]\{A_i\} + \left[F_e^{bx}\right]\{F_{\ell i}\} \\ &+ \left[F_e^{sx}\right]\{X_i\}\; e = 1, .., N_v^e \end{aligned} \tag{54}$$

The above physical-mathematical model describing the effects of the electromagnetic field depending on the fluid flow is formulated for FEM processing [33], utilizing eqs. ((4) and (29)–(34) and (39)–(42)9-50), by the Galerkin method. An open system and the ANSYS environment were applied to deliver the model. The dependencies and functions outlined below were tested, solved, and analyzed in the ANSYS system, and the finite volume method was employed for their formulation in some cases [34].

3. Evaluating the desired functions

The functionality of the numerical model was verified on a DN-100 standard flow meter, with multiple quantities evaluated, compared, and measured.

In the numerical model, we evaluate the voltage on the terminals of E_1 a E_2

$$U_L \cong \sum_{e=1}^{N_\Omega} \left(\frac{\mathbf{J}_e(\mathbf{v})}{I_L} \times \mathbf{B}_e\right) \cdot (\mathbf{v}_{io} + \mathbf{v})_e \Delta V_e, \tag{55}$$

where ΔV_e is the element volume of the discretized area Ω, and N_Ω denotes the number of elements of the area Ω. Assuming that the current density is given by the motion of the positive and negative ions which do not recombine, we can express the current density as

$$\mathbf{J} = \frac{N_q \Delta q}{S\, \Delta t}\mathbf{n}\,, \tag{56}$$

where N_q stands for the number of charges *q*, Δq represents the change of

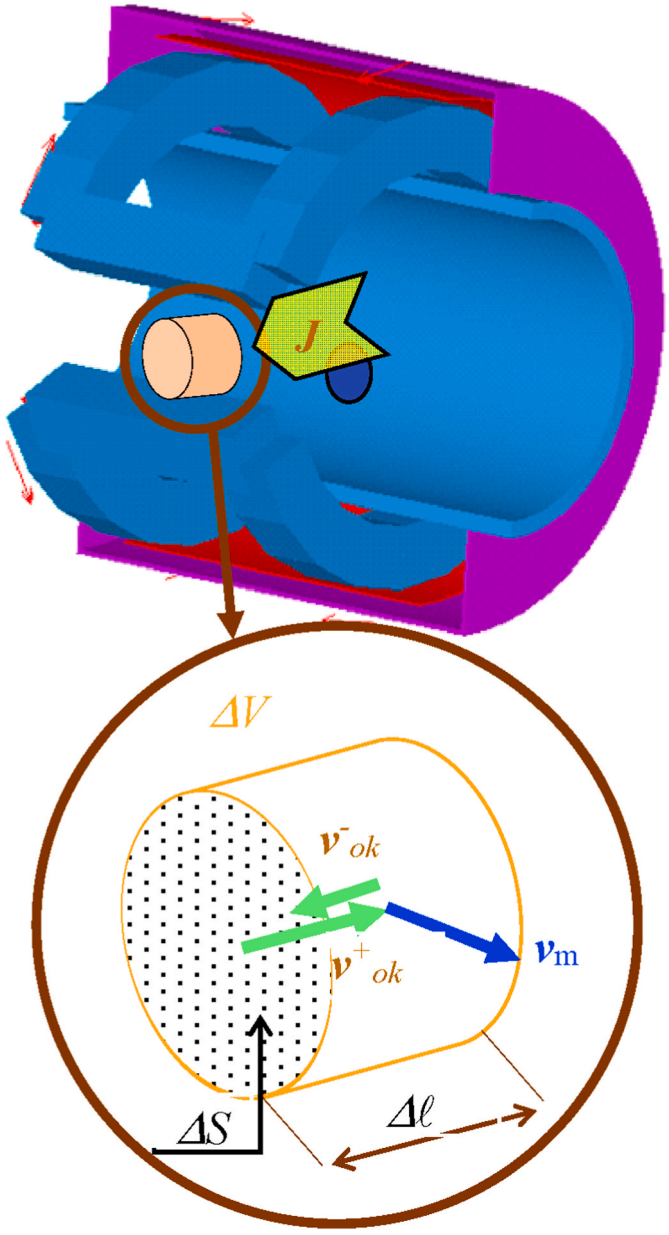

Fig. 4. A geometric model of the flowmeter body.

an elementary charge q, Δt is the time instant, and S denotes the cross-section where the charges q are in motion. Considering the number of ions with a positive or a negative charge, we can express the immediate velocity of the motion $\boldsymbol{v}_{\mathrm{ok}}$, obtaining the current density

$$J = \frac{\sum_{i=1}^{N^+} q_i^+ + \sum_{j=1}^{N^-} q_j^-}{\Delta V} v_{ok}\,, \tag{57}$$

where ΔV is the volume element, N^+ represents the number of positive charges q^+, and N^- denotes the number of negative charges q^- [8,20,21,29] (Fig. 4). In Fig. 4, $\boldsymbol{v}_{\mathrm{m}}$ refers to the immediate velocity of the measured fluid, $\boldsymbol{v}^-_{ok}$ is the immediate velocity of the negative charges, and $\boldsymbol{v}^+_{ok}$ denotes the immediate velocity of the positive charges.

The current density (56) is rewritten as

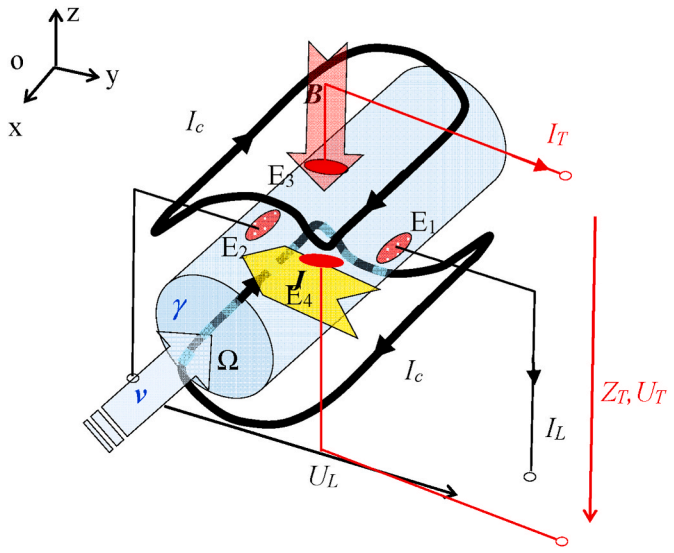

Fig. 5. The principal configuration of the modified inductive flowmeter.

$$\mathbf{J} = \frac{\sum_{i=1}^{N^+} q_i^+ \left(\frac{\mathbf{v}^+_{ok,i}}{\sqrt{\left(|\mathbf{v}_{m,i}|^2 + |\mathbf{v}^+_{ok,i}|^2\right)}} \right)}{2\,\Delta V} + \frac{\sum_{j=1}^{N^-} q_j^- \left(\frac{\mathbf{v}^-_{ok,j}}{\sqrt{\left(|\mathbf{v}_{mj}|^2 + |\mathbf{v}^-_{ok,j}|^2\right)}} \right)}{2\,\Delta V}. \tag{58}$$

The formula for the voltage on the terminals of the electrodes from (55) reads

$$U_L \cong \sum_{e=1}^{N_\Omega} \left(\begin{array}{l} \frac{1}{2I_L} \sum_{i=1}^{N^+} q_i^+ \left(\frac{\mathbf{v}^+_{ok,i}}{\sqrt{\left(|\mathbf{v}_{m,i}|^2 + |\mathbf{v}^+_{ok,i}|^2\right)}} \right) \times \mathbf{B}_e \\ + \frac{1}{2I_L} \sum_{j=1}^{N^-} q_j^- \left(\frac{\mathbf{v}^-_{ok,j}}{\sqrt{\left(|\mathbf{v}_{m,j}|^2 + |\mathbf{v}^-_{ok,j}|^2\right)}} \right)_e \times \mathbf{B}_e \end{array} \right) \cdot \left(\frac{\left(\mathbf{v}^+_{ok} + \mathbf{v}^-_{ok}\right)}{2} + \mathbf{v}_m \right)_e . \tag{59}$$

If we consider the effect of a moving electric charge and the impact of a magnetic field on a charge in motion, then the voltage on the electrodes E_1, E_2 from (17) equals

$$U_L = \iiint_{\Omega} \left(\frac{J(v)}{I_L} \times B \right) \cdot (v_{io} + v_m)\ dV + U_H, \tag{60}$$

where U_H is the electric voltage. After evaluating the U_H in equation (60), we get

$$\begin{aligned} U_L &= \iiint_{\Omega} \left(\frac{\boldsymbol{J}(\boldsymbol{v})}{I_L} \times \boldsymbol{B} \right) \cdot (\boldsymbol{v}_{io} + \boldsymbol{v}_m)\ dV + \iiint_{\Omega} \left(\frac{\boldsymbol{J}(\boldsymbol{v})}{I_L} \times \boldsymbol{B} \right) \cdot (\boldsymbol{v}_{io})\ dV \\ U_L &= \iiint_{\Omega} \left(\frac{\boldsymbol{J}(\boldsymbol{v})}{I_L} \times \boldsymbol{B} \right) \cdot (2\boldsymbol{v}_{io} + \boldsymbol{v}_m)\ dV \end{aligned} \tag{61}$$

The voltage is rewritten for the numerical solution according to (58), yielding

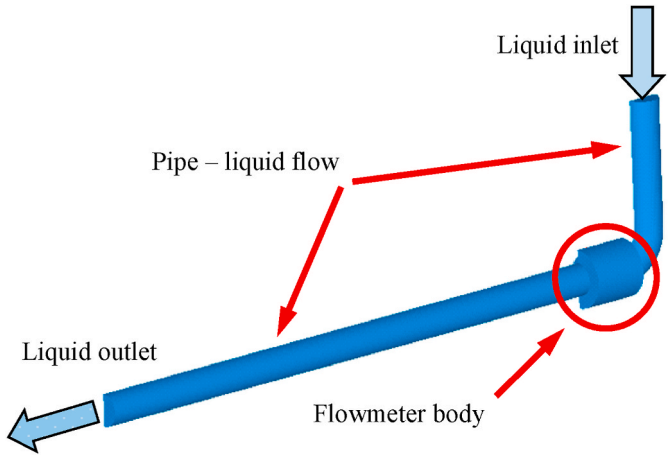

Fig. 6. An inductive flowmeter geometric model: a pipe with the angle of 90°.

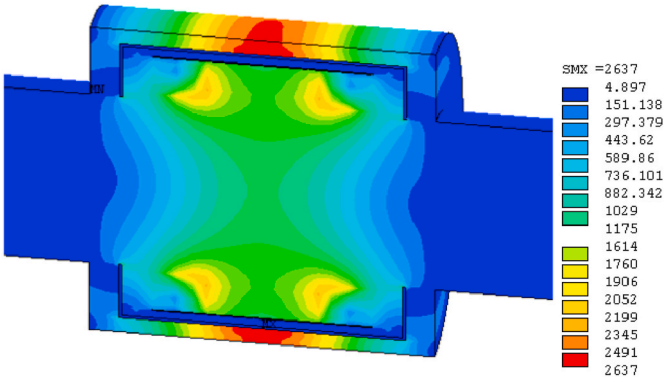

Fig. 7. The magnetic field intensity H [A/m] distribution in the flowmeter body.

$$U_L \cong \sum_{e=1}^{N_\Omega} \left(\begin{array}{l} \dfrac{1}{2\,I_L} \displaystyle\sum_{i=1}^{N^+} q_i^+ \left(\dfrac{\left(\boldsymbol{v}_{ok,i}^+\right)^2}{\sqrt{\left(|\boldsymbol{v}_{m,i}|^2 + \left|\boldsymbol{v}_{ok,i}^+\right|^2\right)}} \right) \times \boldsymbol{B}_e \\ + \dfrac{1}{2\,I_L} \displaystyle\sum_{j=1}^{N^-} q_j^- \left(\dfrac{\left(\boldsymbol{v}_{ok,j}^-\right)^2}{\sqrt{\left(|\boldsymbol{v}_{m,j}|^2 + \left|\boldsymbol{v}_{ok,j}^-\right|^2\right)}} \right)_e \times \boldsymbol{B}_e \end{array} \right) \cdot \left(\boldsymbol{v}_{ok}^+ + \boldsymbol{v}_{ok}^- + \boldsymbol{v}_m\right)_e \tag{62}$$

Possible spurious effects can be suppressed by means of a differential measurement method (Fig. 5). In the lengthwise direction of the electrodes E_1, E_2, we measure the impedance of the fluid as

$$Z_L = f(v, B, \gamma), \tag{63}$$

and in the cross-direction of the electrodes E_3, E_4 then

$$Z_T = f(v, \gamma). \tag{64}$$

4. Geometric model

The geometric model of the flowmeter is characterized in Fig. 3 above. Three functional variants were considered: a solution with a circular inlet pipe (Fig. 6) causing a turbulent flow in the area of the flowmeter; an embodiment utilizing the angle of 0°, 45° (or 90°) between the inlet pipe and the lengthwise direction of the flowmeter; and a straight pipe version.

The ANSYS-BASED FEM/FVM model, described in detail above, was designed for the dynamic condition (via the APDL language) to facilitate the analyses of the current and magnetic fields and fluid velocity distribution by means of the finite element method. In the areas Ω, we evaluated equation (61), which is substituted for the numerical model of the mesh elements.

The main APDL-based model was formulated according to equations (34), (42) and (55), by using tools such as SOLID236 (237), SOLID122 (123), SOLID96, SOURCE36, and FLUID142. The obtained solution relates to the steady state, with respect to the boundary conditions (26),

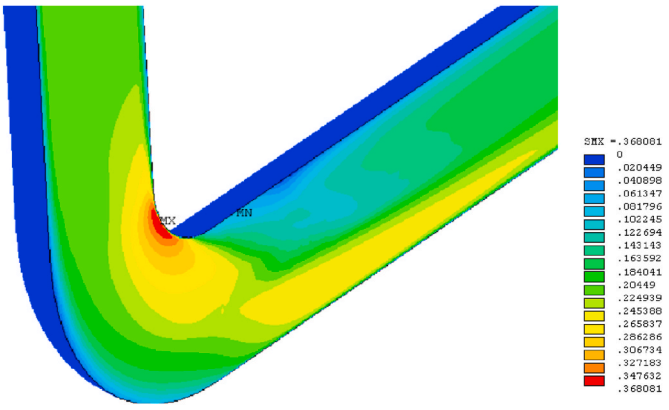

Fig. 8. The distribution of the module of velocity v [m/s] in the fluid: the variant with 90°.

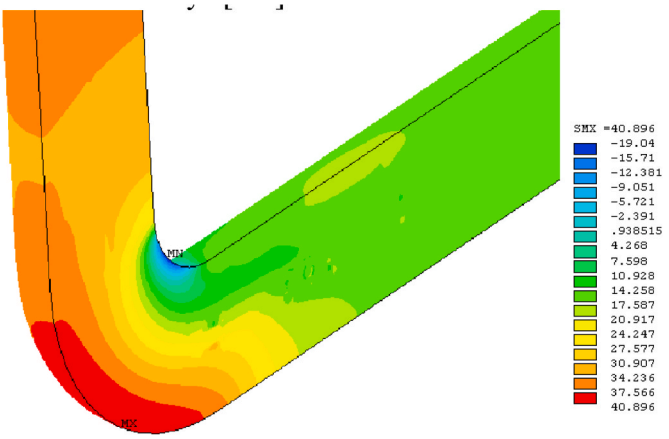

Fig. 9. The pressure distribution p [Pa] in the fluid: the variant with 90°.

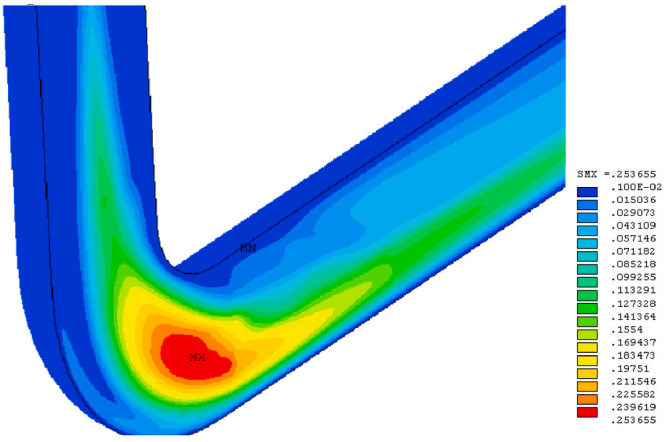

Fig. 10. The dynamic viscosity μ_p distribution in the fluid: the variant with 90°.

Table 1
The physical-chemical composition of the fluid: the volume density.

Substance	Volume density m_{io} [mg·dm^{-3}]
Positive ions	
Na^{I+}	32.71
K^{I+}	1.53
Mg^{II+}	43.81
Ca^{II+}	157.70
Negative ions	
F^{I-}	1.58
Cl^{I-}	5.35
SO_4^{II-}	13.08
NO_3^{I-}	0.54
HCO_3^{I-}	762.40
Neutral substances	
CO_2	4063
H_2O	1,000,000

Table 2
The physical-chemical composition of the fluid: the molar mass.

Substance	Molar mass M_{mo} [g·mol^{-1}]
Positive ions	
Na^{I+}	22.990
K^{I+}	39.102
Mg^{II+}	24.312
Ca^{II+}	40.080
Negative ions	
F^{I-}	19.998
Cl^{I-}	35.453
SO_4^{II-}	32.064 + 4·15.999
NO_3^{I-}	14.007 + 3·15.999
HCO_3^{I-}	1.008 + 12.011+3·15.999
Neutral substances	
CO_2	12.011 + 2·15.999
H_2O	2·1.008 + 15.999

(27), (37), (38), (51), and (52). The coupled model, solved via the sequential method, was initialized and controlled with the help of the APDL language in ANSYS [10].

We computed the flowmeter models for the velocity distribution within the ranges $v = 0.5$–12 m/s and $v = 0.01$–0.5 m/s.

The pipe walls were simulated such that the pressure losses and other parameters exhibited the following values: $K = 0.003$ m^{-1}, $C = 0.999$–0.989, $D_h = 0.05$ m, $a = 0.013$, $b = 0.25$, $\rho = 998$ kg m^{-3}, $\mu_p = 0.001$ kg·m^{-1}s^{-1}, $\nu = 1{\cdot}10^{-6}$ m^2 s^{-1}, $T_0 = 20$ °C. To analyze the magnetic field, we set $I_c = 100$ Az. Further, for the given purpose, $\mu_{r1} = 8000$ was used in the magnetic yoke; $\mu_{r2} = 1000$ in the external magnetic shielding; and $\mu_{r3} = 1$ in air and other diamagnetic materials.

The models enabling us to analyze the current field were solved at $I_{Lstatic} = 171$ mA, $\gamma = 1$ S m^{-1}.

5. Model evaluation

In the magnetic field analysis, we evaluated the flux density B and the field intensity H; the module H is shown in Fig. 7.

The main characteristics of the turbulent flow and the distribution of the velocity, pressure, and dynamic viscosity are displayed in Figs. 8–10; all of the results were evaluated for the mean velocity value of $v = 0.2$ m/s.

As regards the evaluation of the voltage on the terminals of the electrodes E1, E2, the procedure depends on the mean value of the fluid velocity v and the pressure losses in the pipe, without considering the impact of the velocity on the current density distribution $\boldsymbol{J}$ [29].

The voltage is given as

$$U_L \cong \sum_{e=1}^{N_\Omega} \left(\frac{\boldsymbol{J}_e}{I_L} \times \boldsymbol{B}_e \right) \cdot \boldsymbol{v}_e \Delta V_e, \text{ or} \tag{65}$$

Table 3
The physical-chemical composition of the fluid: the substance concentration.

Substance	Concentration c_k [mol·dm^{-3}]
Positive ions	
$c_{1,Na}$	$1.39192{\cdot}10^{-3}$
$c_{2,K}$	$3.83612{\cdot}10^{-5}$
$c_{3,Mg}$	$1.80199{\cdot}10^{-3}$
$c_{4,Ca}$	$3.93463{\cdot}10^{-3}$
Negative ions	
$c_{5,F}$	$8.31648{\cdot}10^{-5}$
c_{6,Cl^-}	$1.80904{\cdot}10^{-4}$
$c_{7,SO4}^-$	$2.04382{\cdot}10^{-4}$
$c_{8,NO3}$	$8.708989{\cdot}10^{-6}$
$c_{9,HCO3}^-$	$12.494000{\cdot}10^{-3}$
Neutral substances	
c_{CO2}	$92.3200{\cdot}10^{-3}$
c_{H2O}	$2.47038{\cdot}10^{5}$

$$U_L \cong \frac{1}{2\,I_L} \sum_{e=1}^{N_\Omega} \left(\left[\begin{array}{l} \displaystyle\sum_{i=1}^{N^+} q_i^+ \left(\frac{\left|\mathbf{v}_{ok,i}^+\right| \, \mathbf{v}_{ok,i}^+}{\sqrt{\left(\left|\mathbf{v}_{m,i}\right|^2 + \left|\mathbf{v}_{ok,i}^+\right|^2 \right)}} \right) \\ \\ + \displaystyle\sum_{j=1}^{N^-} q_j^- \left(\frac{\left|\mathbf{v}_{ok,i}^-\right| \, \mathbf{v}_{ok,i}^-}{\sqrt{\left(\left|\mathbf{v}_{m,j}\right|^2 + \left|\mathbf{v}_{ok,j}^-\right|^2 \right)}} \right) \end{array} \right]_e \times \mathbf{B}_e \right) \cdot \left(\mathbf{v}_{ok}^+ + \mathbf{v}_{ok}^- + \mathbf{v}_m \right)_e . \tag{66}$$

The last formula (66) is required to respect the physical-chemical composition of the fluid. The ion composition of potable water is indicated in Table I (volume density m_{io}) and Table II (molar mass M_{mo}).

According to Refs. [24–36], we can modify equation (66) upon considering the condition of neutrality and regular distribution of ions in the fluid.

We have

$$U_L \cong \frac{1}{2\,I_L} \sum_{e=1}^{N_\Omega} \left(\left[\begin{array}{l} q_e^+ \left(\dfrac{\left|\mathbf{v}_{ok,i}^+\right| \, \mathbf{v}_{ok,i}^+}{\sqrt{\left(\left|\mathbf{v}_{m,e}\right|^2 + \left|\mathbf{v}_{ok,e}^+\right|^2 \right)}} \right) + \\ \\ q_e^- \left(\dfrac{\left|\mathbf{v}_{ok,i}^-\right| \, \mathbf{v}_{ok,i}^-}{\sqrt{\left(\left|\mathbf{v}_{m,e}\right|^2 + \left|\mathbf{v}_{ok,e}^-\right|^2 \right)}} \right) \end{array} \right] \times \mathbf{B}_e \right) \cdot \left(\mathbf{v}_{ok,e}^+ + \mathbf{v}_{ok,e}^- + \mathbf{v}_{m,e} \right) \tag{67}$$

$$\boldsymbol{v}_{ok,e}^+ = \frac{\boldsymbol{E}_e \gamma}{F_c \, \Delta V_e \sum_{k=1}^{N_{ion+}} c_k^+ N_k^{+ion}}, \; \boldsymbol{v}_{ok,e}^- = \frac{\boldsymbol{E}_e \gamma}{F_c \, \Delta V_e \sum_{k=1}^{N_{ion-}} c_k^- N_k^{-ion}}, \tag{68}$$

$$q_e^+ = F_c \, \Delta V_e \sum_{k=1}^{N_{ion+}} c_k^+ N_k^{+ion}, \tag{69}$$

$$q_e^- = F_c \, \Delta V_e \sum_{k=1}^{N_{ion-}} c_k^- N_k^{-ion}, \tag{70}$$

where F_c is the Faraday constant, $F_c = 96{,}484$ C mol^{-1}; $\boldsymbol{E}_e$ denotes the electric field intensity in the direction of the ions' motion in an element of mesh; c^+ represents the positive ions' concentration; c^- stands for the negative ions' concentration; ΔV_e is the element volume; N_k^{+ion} denotes the integer multiple of the electron charge for a specific positive ion; N_k^{-ion} is the integer multiple of the electron charge for a specific negative ion; q_e^- represents the whole charge of negative ions in one element; q_e^+ is the whole charge of positive ions in one element; N_{ion+} stands for the number of different positive charge carriers (elements, compounds); and

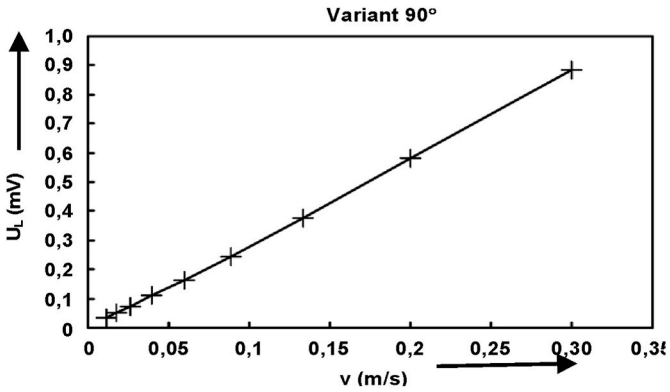

Fig. 11. The relationship between the flowmeter voltage and the flow velocity: the 90° variant (the results obtained from the numerical model).

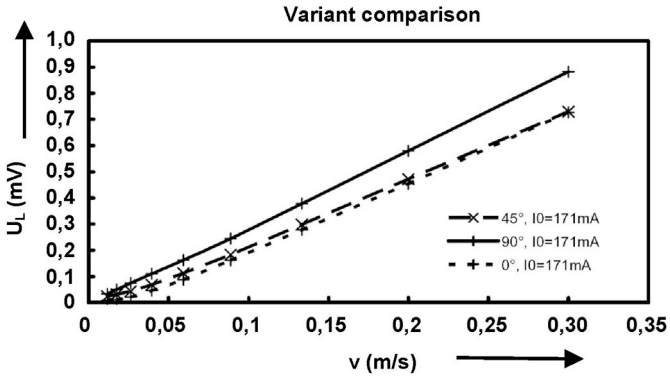

Fig. 12. The relationships between the flowmeter voltage and the flow velocity compared: the 0°, 45°, and 90° versions (the results obtained from the numerical model).

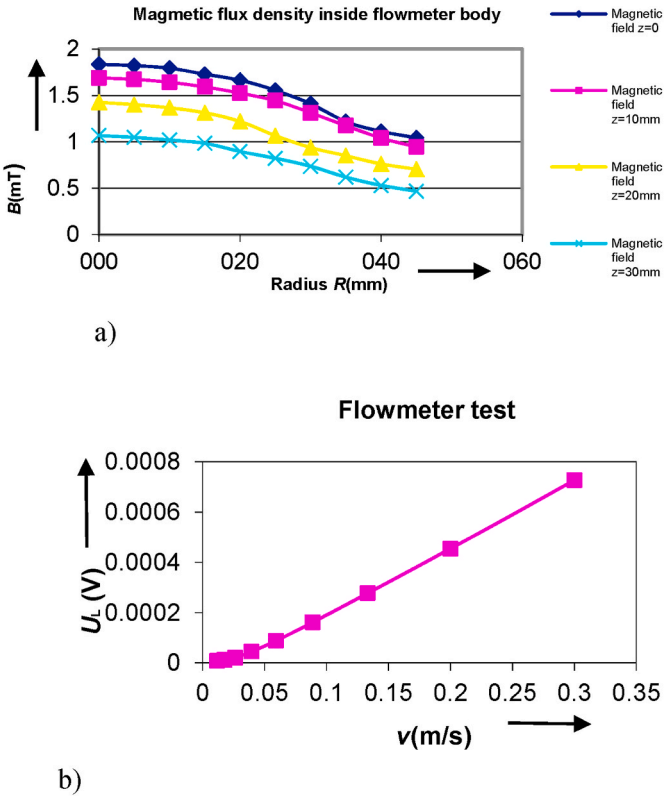

Fig. 14. The experimental flowmeter measurement: a) the magnetic field; b) the testing of the impact exerted by the voltage U_L on the flow velocity v.

N_{ion-} is the number of different negative charge carriers (elements, compounds). The concentration of ions in the fluid is given by

$$c_k = \frac{m_{io,k}}{M_{mo,k}} \quad k = 1, .., N_{ion}. \tag{71}$$

The values of the concentration c_k in the fluid are summarized in Table III.

The above formulas (67) - (71) yield the voltage

Fig. 13. The experimental testing of the flowmeter body: a) open; b) magnetic field verification.

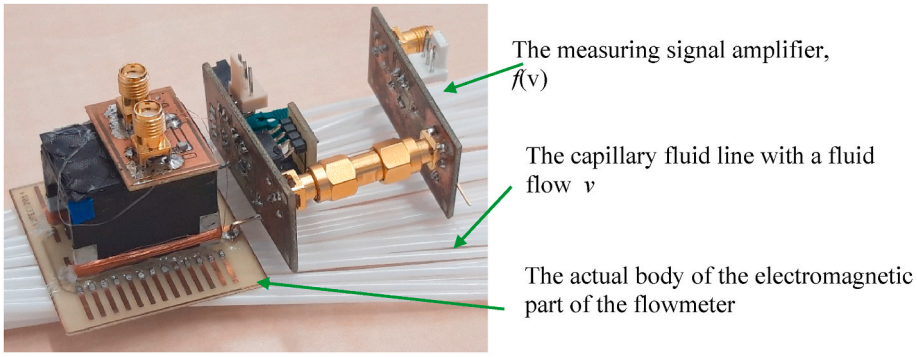

Fig. 15. The configuration of the experimental flowmeter to measure flow velocities within $\boldsymbol{v} = 0.0005–0.01$ m/s.

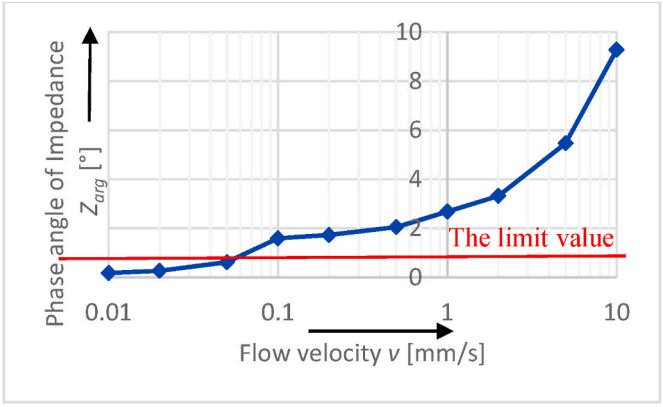

Fig. 16. The experimental flowmeter measurement and tests of the relationship between the impedance phase of $\underline{Z}$ and the flow velocity $\boldsymbol{v}$.

$$U_L \cong \left(\frac{1}{|ik^+|}+\frac{1}{|ik^-|}\right)\cdot\left(\mathbf{J}_e\left(\frac{1}{|ik^+|}+\frac{1}{|ik^-|}\right)+\Delta V_e F_c \mathbf{v}_{m,e}\right) \cdot\frac{1}{2\,F_c^2 I_L}\cdot(\mathbf{J}_e\times\mathbf{B}_e)\cdot\sum_{e=1}^{N_\Omega}\frac{|\mathbf{J}_e|}{\Delta V_e^2\sqrt{\left(|v_{m,e}|^2+\left(\frac{|\mathbf{v}^+_{ok,e}|+|\mathbf{v}^-_{ok,e}|}{2}\right)^2\right)}} \tag{72}$$

$$\mathbf{v}^+_{ok,e}=\frac{\mathbf{J}_e}{F_c\,\Delta V_e ik^+},\ \mathbf{v}^-_{ok,e}=\frac{\mathbf{J}_e}{F_c\,\Delta V_e ik^-}, \tag{73}$$

$$ik^+=\sum_{k=1}^{N_{ion+}} c_k^+ N_k^{+ion}=1,2902\cdot10^{-5}\ \ \mathrm{mol/m^{-3}},$$

$$ik^-=\sum_{k=1}^{N_{ion-}} c_k^- N_k^{-ion}=-1,3175\cdot10^{-5}\ \ \mathrm{mol/m^{-3}}, \tag{74}$$

where ik^+ and ik^- denote the concentrations of all positive and negative ions, respectively. Equation (72) will then be simplified with respect to electric neutrality [29].

6. Discussion

The results obtained from an analysis of the three geometrical configurations of the pipe are presented and compared below, Figs. 11 and 12. The low-velocity test of the fluid flow was solved for $v = 0.01–0.3$ m $\cdot s^{-1}$. The partial experimental verifications [29] are shown in Figs. 11, 13 and 14.

One of the central steps in the entire set of procedures relating to the flowmeter consisted in designing the device's special structure; most importantly in this context, the device was arranged to sense velocity v up to a distance of 5 mm from the surface of the body, within the mean velocity range of liquid $v = 0.01–1.0$ mm/s (contact design - Fig. 15). The concept corresponds to the intended use in the non-destructive sensing of fluid velocity in the xylem of plants and trees [18,19]. The electromagnetic part was designed to provide a measurable electrical signal at the maximum possible value, as a function of velocity f(v). The signal thus obtained is then pre-amplified to the required level on the flowmeter body and then further processed via standard methods (Fig. 15).

We configured the flowmeter to measure ultra-low velocity fluid flow by exploiting the above-presented numerical model. The flowmeter operates via transimpedance measurement in the resonant mode. The special structural concept (Fig. 15 [29]) suitable for the fluid flow within the mean velocity range of $v = 0.01–1.0$ mm/s enables contact fluid flow measurement, as already indicated. Fig. 15 displays in detail the structure and test configuration of the apparatus to determine the limit value of mean velocity v_{min}.

The flowmeter, Fig. 15, provided a lower measured velocity value of $v_{min} = 50.10^{-6}$ m/s, (Fig. 16); this value was achieved in the evaluation of impedance $\underline{Z}$ (75), namely, its phase component Z_{arg}

$$\underline{Z}=\frac{\underline{Z}_v H\,\Delta\ell}{\underline{J}\cdot\Delta S}, \tag{75}$$

Table 4
The flow rates measured via the resonance principle.

Flow rate, v [mm/s]	Time shift $\lvert\Delta x\rvert$ [ns]	Phase shift [°]
10.00	263.0	9.279
5.00	155.0	5.468
2.00	94.0	3.316
1.00	71.0	2.681
0.50	58.0	2.046
0.20	49.0	1.729
0.10	45.0	1.588
0.05	17.5	0.617
0.02	7.5	0.265
0.01	5.0	0.176
0.00	6.0	0.212

Table 5
The uncertainties A, B, and C evaluated in testing the sample flowmeter.

v [mm/s]	u_{AX}	u_{BX}	u_C
10.00	0.17463	0.04236	0.17969
5.00	0.34925	0.04203	0.35177
2.00	0.69851	0.02147	0.69884
1.00	0.17463	0.02142	0.17594
0.50	0.17463	0.02136	0.17593
0.20	0.34925	0.02133	0.34991
0.10	0.17463	0.01114	0.17498
0.05	0.12224	0.01105	0.12274

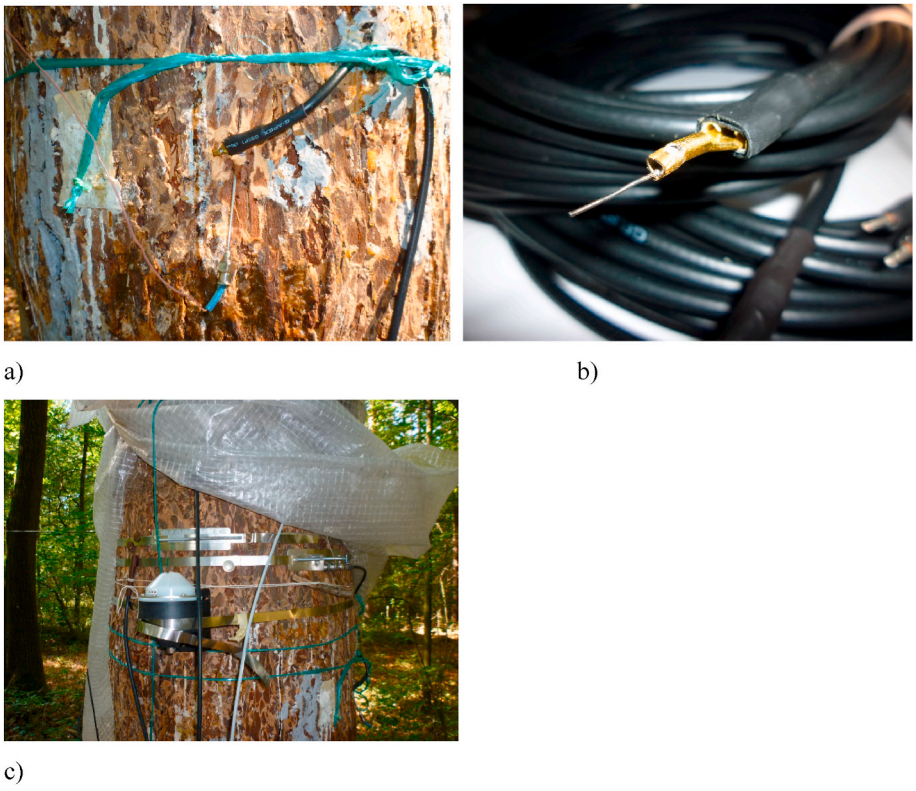

Fig. 17. The current methods for the semi-destructive measurements of fluid flow rates in trees: a) the semi-destructive calorimetric technique; b) a part of the sensor facilitating semi-destructive measurement; c) application on a test tree.

where $\underline{H}$ is the magnetic field intensity in the complex form, $\underline{Z}_v$ is the wave impedance, $\underline{\boldsymbol{J}}$ denotes the current density in the complex form, $\Delta \boldsymbol{S}$ stands for the surface element vector, and $\Delta \ell$ is the tangential element of length. The above-formulated relationships were obtained through FEM-based numerical modeling in the ANSYS system [9,21,30–32]. The relevant analysis then yielded the required metrological characteristics and corresponding procedures to be adopted for the measurement of low-level liquid flows. When evaluating the module of impedance $|\underline{Z}| = Z_{mod}$ and its phase $\underline{Z}\angle\arg = Z_{arg}$, we can obtain the required measurement sensitivity and accuracy; advantageously, it is possible to exploit the near-resonance state, where the sensitivity of the impedance components to a flow velocity change increases markedly.

The flowmeter was subjected to repeated sensing tests combined with monitoring the flow velocity within the range of $v = 0.01–10$ mm/s. The measurement and evaluation data are summarized in Table IV. Subsequently, we compiled Table V to comprise the measurement uncertainties A, B, and C for the relevant measuring cycles, Table IV.

In the uncertainty A, the measurement was carried out in two instances, with the expansion coefficient $k_S = 7$; as regards the uncertainty B, we evaluated (Table IV) the impact of the oscilloscope on the measured quantity.

The flowmeter designed and experimentally verified as shown herein is suitable for the basic non-destructive measurement discussed within sources [18,19], Fig. 17.

7. Conclusion

This paper discusses diverse aspects of the design, numerical modeling, and experimental verification of an inductive flowmeter. The device was tested and experimentally verified for use with a pipe having a diameter of $R = 100$ mm; however, extreme or contact conditions were also assumed. We evaluated the physical-mathematical and numerically modeled design by using a geometric model created in the ANSYS system; the numerical model included the impact of turbulent flow, pressure losses in the wall, and the chemical composition of the fluid, all factor obtained via the FEM/FVM. The numerical versions were tested in three geometric configurations: The first embodiment used a straight tube showing $-0°$, while the other two tubes were bent at $-45°$ and $90°$; the properties of the individual options are compared in Fig. 12. The proposed flow meter was then subjected to experimental measurements. The maximum variation of the simulated flowmeter characteristics with respect to the measured ones (Figs. 11 and 12) did not exceed 3% [21]. The flowmeter for extremely low flow rates v in the range of $v = 0.01–1.0$ mm/s was not only modeled according to a verified electromagnetic model but also experimentally assembled and tested. During the initial laboratory measurements and functionality verification, the limit speed of 50 μm/s was reached and the measurement uncertainty evaluated for contact, which attained 20% within the limits of the lower speed interval.

The concept proved applicable in dendrology [18] and is being further developed and refined to allow large-scale comparison with the semi-destructive methods currently in use on test trees. Importantly, the device embodies a significant shift in the accuracy and repeatability of flow measurement (considering its non-destructive character), compared to the methods used thus far [19].

The flowmeter is capable of measuring flows in selected/special media (Argon, Nitrogen) at different temperatures in a wide range (approx. 200 K). The data obtained on flows with small values of the medium velocity v are beneficial in special cryogenic applications.

The research is based on the state of the art in inductive flowmeters [35,36], namely, devices whose use is associated with analyzing the combined electromagnetic field - fluid flow and evaluating the sensitivity and rate of the impact on the measurement accuracy.

Author contributions

P.F. contributed to the theoretical section, numerical model, and

experiments; he also wrote the paper; R.K., P.L., M.K. conceived and designed the experiments; T.M. contributed to the optimization procedures of numerical models; J.Z. and P.D. evaluated the experiments and graphics.

Declaration of competing interest

The authors declare no conflict of interest. The founding sponsors had no role in the design of the study; in the collection, analyses, or interpretation of data; in the writing of the manuscript, and in the decision to publish the results.

Acknowledgements

The research was funded via a grant of Czech Science Foundation (GACR 20-14105S) and the grant BD 2020–2020 FEKT-S-20-6360. For the actual analyses and experiments, the infrastructure of the SIX Center was used.

References

[1] R. Van der Pol, Session E, Paper E-2, in: Hungary Budapest, Akademiai Kiado (Eds.), Measurements on a Magnetic - Inductive Flowmeter for Very Low Conducting Fluids, 1983, pp. 73–84.
[2] J. Delsing, K. Karlsson, Low-pressure gap discharge ultrasonic gas flowmeter, in: Paper Presented at the 15th International Flow Measurement Conference 2010, FLOMEKO 2010, 2010, pp. 259–266, 2010.
[3] J. Zakrzewski, Accuracy in analytical measurements, in: Measurement 2011, Proceedings of the 8th International Conference, Smolenice, Slovakia, 2011, pp. 20–23.
[4] N. Bignell, Y.M. Choi, Thermal effects in small sonic nozzles, Flow Meas. Instrum. 13 (1–2) (2002) 17–22, https://doi.org/10.1016/S0955-5986(02)00012-2.
[5] M. Li, M. Henry, F. Zhou, M. Tombs, Two-phase flow experiments with coriolis mass flow metering using complex signal processing, Flow Meas. Instrum. (2019) 69, https://doi.org/10.1016/j.flowmeasinst.2019.101613.
[6] T.T. Yeh, G.E. Mattingly, Pipeflow downstream of a reducer and its effects on flowmeters, Flow Meas. Instrum. 5 (3) (1994) 181–187, https://doi.org/10.1016/0955-5986(94)90017-5.
[7] R.O. Webilor, G.P. Lucas, M.O. Agolom, Fast imaging of the velocity profile of the conducting continuous phase in multiphase flows using an electromagnetic flowmeter, Flow Meas. Instrum. 64 (2018) 180–189, https://doi.org/10.1016/j.flowmeasinst.2018.10.024.
[8] J.A. Stratton, Electromagnetic Theory, McGraw-Hill Boook Company, USA, 1941.
[9] ANSYS manuals, USA, www.ansys.com (accessed 1994-2020).
[10] I.A. Maalouf, The derivation and validation of the practical operating equation for electromagnetic flowmeters: case of having an electrolytic conductor flowing through, IEEE Sensor. J. 6 (1) (2006) 89–96.
[11] I.A. Maalouf, A valid model for the electromagnetic flowmeter's measuring: case of having an electrolytic conductor flowing through, IEEE Sensor. J. 6 (3) (2006) 623–630.
[12] U.R. Prasanna, L. Umanand, Non-disruptive and null-deflection mass flow measurement by a pressure compensation technique, Flow Meas. Instrum. 21 (1) (2010) 54–61.
[13] Y. Chen, Y. Chen, S. Hu, Z. Ni, Continuous ultrasonic flow measurement for aerospace small pipelines, Ultrasonics (2021) 109, https://doi.org/10.1016/j.ultras.2020.106260.
[14] J. Geršl, S. Knotek, Z. Belligoli, R.P. Dwight, R.A. Robinson, M.D. Coleman, Flow rate measurement in stacks with cyclonic flow – error estimations using CFD modelling, Measurement: Journal of the International Measurement Confederation 129 (2018) 167–183.
[15] A. Thöne, R. Bensch, Professional alternating field technology. Magnetic-inductive measurement of flow in rough applications in the paper industry, Wochenblatt fuer Papierfabrikation 134 (23–24) (2006) 1434–1435.
[16] Y.Y. Shi, M. Wang, Analytical investigation of an inductive flow sensor with arc-shaped electrodes for water velocity measurement in two-phase flows, Flow Meas. Instrum. 41 (2015) 90–96.
[17] C. Xu, S. Wang, G. Tang, D. Yang, B. Zhou, Sensing characteristics of electrostatic inductive sensor for flow parameters measurement of pneumatically conveyed particles, J. Electrost. 65 (9) (2007) 582–592.
[18] J. Cermak, N. Nadezhdina, Application of a sap flow technique for characterizing the whole tree architecture, crowns and roots, Acta Hortic. 846 (2009) 219–228, https://doi.org/10.17660/ActaHortic.2009.846.23.
[19] M. Trcala, J. Cermak, A new heat balance equation for sap flow calculation during continuous linear heating in tree sapwood, Appl. Therm. Eng. 102 (2016) 532–538.
[20] P. Fiala, Model of Inductive Flowmeter DN-100. Research Report no.2/01, Laboratory of modelling and optimisation of electromechanical systems BUT FECT, Brno, Czech Republic, 2001, pp. 1–23.
[21] P. Fiala, T. Jirku, I. Behunek, Numerical Model of Inductive Flowmeter, 2007, pp. 971–975. PIERS2007, Beijing, 1559-9450.
[22] I. Burian, L. Dedek, J. Dedkova, Analysis and optimization of an inductive flowmeter, in: In Proc. 8th International Symposium on Theoretical Electrical Engineering, Thessaloniki, 1995, pp. 506–509.
[23] P. Fleichschner, Hydromechanics. Brno, Czech Republic, FME Brno University of Technology, 1990.
[24] C.E. Agu, Å. Hjulstad, G. Elseth, B. Lie, Algorithm with improved accuracy for real-time measurement of flow rate in open channel systems, Flow Meas. Instrum. 57 (2017) 20–27, https://doi.org/10.1016/j.flowmeasinst.2017.08.008.
[25] J.W. Moore, Physical Chemistry, 1981. Prague, Czech Republic: SNTL.
[26] R. Brdička, J. Dvořák, The Introduction to Physical Chemistry, Academia, Prague, Czech Republic, 1977.
[27] L. Sommer, The Introduction to Analytical Chemistry, Brno University of Technology, Brno, Czech Republic, 1988.
[28] P. Fiala, J. Zukal, Measuring ultra-low fluid flow velocities in the context of industry 4.0, in: Paper Presented at the 2019 International Interdisciplinary PhD Workshop, IIPhDW2019, 2019, pp. 43–46, https://doi.org/10.1109/IIPHDW.2019.8755410.
[29] P. Fiala, R. Kadlec, J. Zukal, Measuring fluid flow velocities in the context of industry 4.0, in: Paper Presented at the 2019 Proceedings of the 12th International Conference on Measurement, MEASUREMENT 2019, 2019, pp. 295–298.
[30] T. Rymarczyk, New methods to determine moisture areas by electrical impedance tomography, Int. J. Appl. Electromagn. Mech. 37 (1–2) (2016) 79–87.
[31] T. Rymarczyk, J. Sikora, Applying industrial tomography to control and optimization flow systems, Open Phys. 16 (2018) 332–345, https://doi.org/10.1515/phys-2018-0046, 2018.
[32] T. Rymarczyk, P. Tchórzewski, J. Sikora, Implementation of electrical impedance tomography for analysis of building moisture conditions, COMPEL 37 (5) (2018) 1837–1861, https://doi.org/10.1108/COMPEL-01-2018-0034.
[33] O. Zienkiewicz, R. Taylor, J.Z. Zhu, The Finite Element Method: its Basis and Fundamentals, seventh ed., 2013, pp. 1–714. The Finite Element Method: its Basis and Fundamentals: Seventh Edition.
[34] S. Delcourte, D. Jennequin, Saddle point preconditioners for linearized Navier-Stokes equations discretized by a finite volume method, Appl. Numer. Math. 60 (11) (2010) 1054–1066.
[35] R.O. Webilor, G.P. Lucas, M.O. Agolom, Fast imaging of the velocity profile of the conducting continuous phase in multiphase flows using an electromagnetic flowmeter, Flow Meas. Instrum. 64 (2018) 180–189.
[36] D.W. Clarke, J. Hemp, Eddy-current effects in an electromagnetic flowmeter, Flow Meas. Instrum. 20 (1) (2009) 22–37.